



Enhancing reactive oxygen species generation and photocatalytic performance via adding oxygen reduction reaction catalysts into the photocatalysts

Shuquan Huang^a, Yuanguo Xu^{a,*}, Qingqing Liu^a, Ting Zhou^a, Yan Zhao^b, Liquan Jing^a, Hui Xu^b, Huaming Li^{b,*}

^a School of Chemistry and Chemical Engineering, School of Pharmacy, Jiangsu University, Zhenjiang 212013, PR China

^b Institute for Energy Research, Jiangsu University, Zhenjiang 212013, PR China

ARTICLE INFO

Article history:

Received 25 March 2017

Received in revised form 6 June 2017

Accepted 11 June 2017

Available online 12 June 2017

Keywords:

Magnetic photocatalyst

Water disinfection

Ag₃PO₄

CoFe₂O₄

ORR

ABSTRACT

In this work, a novel Ag₃PO₄@CoFe₂O₄ composite photocatalyst was synthesized via a phosphate salts alkalinity adjustment strategy. Structure, morphology, and chemical component analysis indicated that the magnetic CoFe₂O₄ nanoparticles (NPs) were evenly decorated on the surface of Ag₃PO₄ particles, forming a sesame ball like structure. This unique structure ensures that the Ag₃PO₄@CoFe₂O₄ composites could be totally separated by the magnet field. Photocatalytic water disinfection and organic pollutants degradation were employed to evaluate the photocatalytic performance of the as-prepared magnetic photocatalysts. The results showed that the optimum 3% Ag₃PO₄@CoFe₂O₄ composite could completely inactivate 1*10⁷ cfu/mL of Escherichia coli within 40 min, much faster than the pristine Ag₃PO₄. Meanwhile, the 3% Ag₃PO₄@CoFe₂O₄ composite also showed a dramatic enhancement of photocatalytic activities for the organic pollutants degradation. The reactive oxygen species yield measurements, O₂ control photocurrents experiments, O₂-TPD tests and photoluminescence spectra analysis indicate that the surface modification of CoFe₂O₄ NPs could facilitate the O₂ adsorption and O—O bond activation/cleavage/oxide removal and accelerate the two-electron oxygen reduction reaction for H₂O₂ generation on the surface of Ag₃PO₄, and thus more ROSs were generated. In addition, due to the acceleration of electrons consumption, more holes will be left for the organic pollutants oxidation, and the photocatalytic activities as well as stability of Ag₃PO₄ therefore have been greatly improved.

© 2017 Elsevier B.V. All rights reserved.

1. Introduction

Photocatalytic solar-energy conversion is being drawn increasing attention due to its robust new methods for water purification and environmental protection at lower cost and energy consumption [1,2]. Commercial TiO₂ has been recognized as efficient photocatalysts for water disinfection and organic pollutant degradation [3]. However, the large value of its bandgap results in the requirement of ultraviolet irradiation, which limit its practical utility for photocatalytic applications [4]. Therefore, the development of visible-light-driven (VLD) photocatalysts is considerably needed. Besides the VLD, reactive oxygen species (ROS), such as the hydroxyl radical, singlet oxygen superoxide, and their generation efficiency also should be involved in the photocatalysts designation

because ROS govern the water purification ability [5–8]. Furthermore, the recyclability and stability of a photocatalyst need to be considered in the concept of “green chemistry” [9]. Upon gathering the above information, to seek novel photocatalysts which possess specific features including large visible light response, high ROS produce ability, easy recyclability and superior stability is extremely attractive.

Silver phosphate (Ag₃PO₄), with a suitable band gap of 2.45 eV and can absorb light that wavelength shorter than ca. 530 nm, has aroused increasing attention due to its excellent quantum efficiency in many photocatalytic fields, such as O₂ evolution from water splitting [10–12], organic pollutants elimination, CO₂ reduction [13] and so on. Up to now, various strategies for improving the activity of Ag₃PO₄ include morphology control to expose high energy surface [14,15], chemical modification to extend the absorption region [16,17], and band alignment by coupling with other semiconductors and co-catalysts to improve the electron–hole separation [18–23]. Despite the growing number of works exploring

* Corresponding authors.

E-mail addresses: xuyg@ujs.edu.cn (Y. Xu), lhm@ujs.edu.cn (H. Li).

these strategies, the literatures have mainly focused on expending the light absorption and charge transfer of Ag_3PO_4 . The researches of improving the surface/interface catalytic reaction efficiency (such as dissolved oxygen reduction and charge consumption) on the surface of Ag_3PO_4 are very rare. While on the one hand, the surface/interface catalytic reaction is an indispensable step of photocatalysis process and it plays a key role in ROS generation [24]. On the other hand, most semiconductor materials are nonspecific in catalyzing ROS production. Therefore, materials specific in catalyzing ROS production need to be combined into Ag_3PO_4 to further promote the photocatalytic activity. As some photocatalysis systems have verified that the introduction of electrocatalysis active materials could boost the ROS generation. For example, Liu et al. [25] showed that with additional catalysts (Cu or Au) were deposited onto the MoS_2 films, the ROS production abilities of $\text{FLV}-\text{MoS}_2$ were greatly enhanced and achieved a rapid water disinfection. And the reasons behind it were the high oxygen active abilities of Cu and Au. Therefore, adding oxygen active materials in Ag_3PO_4 may be an alternative strategy to improve the surface/interface catalytic reaction efficiency. Besides that, the problem of the easy loss of the suspended particulate catalysts in the process of photocatalytic reaction and separation has rarely addressed.

Spinel ferrite CoFe_2O_4 possesses unique magnetic, electric, physical, and chemical properties [26,27], which render it as an ideal candidate of magnetically recoverable catalyst supports [28–34], active material for batteries [35], and biomedical devices [36]. Especially, the recent reports on CoFe_2O_4 for oxygen reduction reaction (ORR), have attracted considerable attention due to their high abundance, low cost and environmental friendliness [37–39]. It is no doubt that the CoFe_2O_4 is an active and robust catalyst for O–O bond activation/cleavage and oxide removal. Accordingly, these superiorities of CoFe_2O_4 motivate us to fabricate $\text{CoFe}_2\text{O}_4/\text{Ag}_3\text{PO}_4$ magnetic photocatalysts with the hope of improving the dissolved oxygen reduction catalytic reactions of Ag_3PO_4 and promoting the production of ROS, as well as recycling the photocatalysts easily. Although, the work about $\text{Ag}_3\text{PO}_4@\text{CoFe}_2\text{O}_4$ magnetic photocatalysts that could enhance the photocatalytic activities towards organic dyes degradation dramatically has been reported [40], the discussion of the possible $\text{Ag}_3\text{PO}_4@\text{CoFe}_2\text{O}_4$ core-shell structure formation mechanisms, the photocatalytic disinfection performance and the specific catalyzing ROS production features of CoFe_2O_4 in the $\text{Ag}_3\text{PO}_4@\text{CoFe}_2\text{O}_4$ composites were firstly discussed in the present literature.

It is well known that human health drinking water must be free of pollutants such as pathogenic bacteria and organics. Usually, the wastewater is complex with different kinds of pollutants [41]. Accordingly, it is urgent to develop a novel photocatalyst that can be used to remove different pollutants simultaneously. Our previous works have developed some magnetic photocatalysts, which have been used for simultaneous bactericidal and organic pollutants removal [32,34,42]. For the purpose of further understanding the photocatalytic mechanism and developing more efficient photocatalysts, in this study, we tactfully utilized the surface-electric properties of the CoFe_2O_4 that can be tuned by the pH adjustment [43]. Taking the strong alkali salt Na_3PO_4 as the source of PO_4^{3-} simultaneously to tune the surface-electric properties of the CoFe_2O_4 negative enough to catch Ag^+ . As a result, the CoFe_2O_4 NPs can attach on the surface of Ag_3PO_4 particles evenly. The followed simple hydrothermal treatment produced uniformed and highly crystallized sesame ball like $\text{Ag}_3\text{PO}_4@\text{CoFe}_2\text{O}_4$ composites. The as-prepared $\text{Ag}_3\text{PO}_4@\text{CoFe}_2\text{O}_4$ composites combined the VLD and excellent photocatalytic activities of Ag_3PO_4 , oxygen active abilities and magnetic property of CoFe_2O_4 , which displayed superior photocatalytic activities in both rapid water disinfection and organic pollutants degradation. By using colorimetric

N, N-diethyl-p-phenylenediamine (DPD) method and ESR analysis, it concludes that the CoFe_2O_4 NPs in the $\text{CoFe}_2\text{O}_4@\text{Ag}_3\text{PO}_4$ composites can act as a specific component in catalyzing ROS (especially H_2O_2 and hydroxyl radical) production. More important, the $\text{CoFe}_2\text{O}_4@\text{Ag}_3\text{PO}_4$ composites can be easily separated via a magnetic field.

2. Experimental section

2.1. Synthesis of CoFe_2O_4 NPs

The CoFe_2O_4 NPs were prepared by a hydrothermal treatment method. In a typical process, 2.304 g $\text{FeCl}_3 \cdot 6\text{H}_2\text{O}$ and 1.010 g $\text{CoCl}_2 \cdot 6\text{H}_2\text{O}$ were dissolved in 30 mL ethanol solution (ethanol: $\text{H}_2\text{O}=3:1$). Then, a certain amount of 28% concentrated ammonia aqueous solution were added slowly into the above solution to make the $\text{pH}>9$, followed by 0.5 h stirring. After that, the suspensions were transferred to a 50 mL stainless steel autoclave with a Teflon liner and kept at 180 °C for 20 h. Subsequently, the stainless steel autoclaves were allowed to cool to room temperature and the precipitates were washed with deionized water until the $\text{pH}=7$. The obtained CoFe_2O_4 NPs were then redispersed in deionized water. Part of CoFe_2O_4 NPs were centrifuged and dried at 60 °C for characterization.

2.2. Synthesis of $\text{Ag}_3\text{PO}_4@\text{CoFe}_2\text{O}_4$ composite material

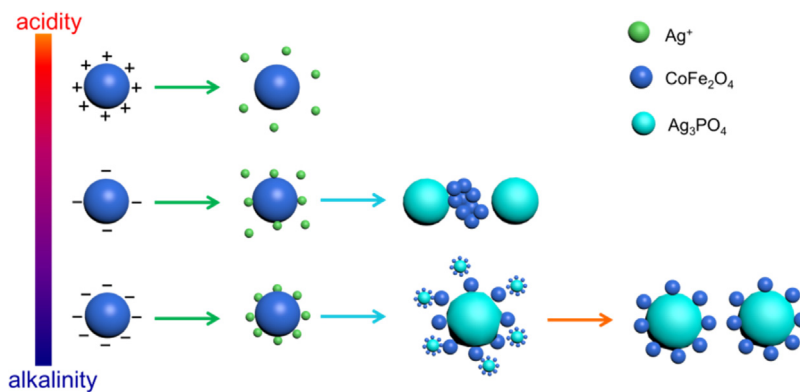
The $\text{Ag}_3\text{PO}_4@\text{CoFe}_2\text{O}_4$ composites were prepared via an in situ precipitation process followed by a simple hydrothermal strategy. Typically, 0.4 g AgNO_3 was dissolved in 30 mL deionized water. Then, a certain amount of above prepared CoFe_2O_4 (0.004 g mL^{-1}) suspensions were added and stirred for 0.5 h. Subsequently, 3 mL Na_3PO_4 solution (1 g mL^{-1}) were added into the mixture drop by drop and kept stirring for 1 h. It should be noted that the whole experiments were kept at 60 °C with a circulating water system. After the precipitation process, the suspension was transferred to several 25 mL Teflon-lined stainless-steel autoclaves and kept for 2 h at 120 °C. After cooling to room temperature, these obtained precipitates were washed with distilled water and ethanol for several times, and then dried at 60 °C in a vacuum oven overnight. The final products were named as 1% $\text{Ag}_3\text{PO}_4@\text{CoFe}_2\text{O}_4$, 3% $\text{Ag}_3\text{PO}_4@\text{CoFe}_2\text{O}_4$ and 5% $\text{Ag}_3\text{PO}_4@\text{CoFe}_2\text{O}_4$ according to the mass fraction of CoFe_2O_4 in the weight of AgNO_3 .

The Ag_3PO_4 (Na_2HPO_4) and $\text{CoFe}_2\text{O}_4/\text{Ag}_3\text{PO}_4$ composite (Na_2HPO_4) were prepared via a similar method except using Na_2HPO_4 instead of Na_3PO_4 and the mass fraction of CoFe_2O_4 in the weight of AgNO_3 was 5%.

The Ag_3PO_4 and $\text{Ag}_3\text{PO}_4@\text{CoFe}_2\text{O}_4$ composites without hydrothermal treatment were remarked as Ag_3PO_4 (Na_3PO_4) and $\text{Ag}_3\text{PO}_4@\text{CoFe}_2\text{O}_4$ composites (Na_3PO_4), respectively.

2.3. Photocatalytic disinfection performance

Escherichia coli (*E. coli*) was used as the target bacterium to evaluate the photocatalytic disinfection performance in this study. Before experiment, all glass apparatuses and culture medium solution used in the experiments were autoclaved at 121 °C for 20 min. The bacterial cells were grown in nutrient broth at 37 °C for 20 h under agitating at 200 rpm to yield a cell count of approximately 10^9 colony forming units (cfu)/mL. Subsequently, the sample was washed three times with bacterial phosphate buffered saline (PBS) solution by centrifugation for 10 min. Then the cell pellet was resuspended in the PBS solution. After that, the cell suspension was added into the pyrex glass reactor which contained 20 mL bacterial PBS solution and the photocatalyst concentration at 10 $\mu\text{g/mL}$. The final cell concentration in the test was adjusted to 10^7 cfu/mL.



Scheme 1. Schematic illustration on the synthetic process for sesame ball like $\text{Ag}_3\text{PO}_4@\text{CoFe}_2\text{O}_4$ composites.

Before irradiation, the suspensions were magnetically stirred for 30 min in the dark in order to keep the adsorption–desorption equilibrium. During the photoreactions ($\lambda > 420 \text{ nm}$ /250 W xenon lamp as the light source), aliquots of the sample were collected and serially diluted with PBS solution. 100 μL samples were then evenly spread on nutrient agar plates and incubated at 37 °C for 24 h in dark.

2.4. Photocatalytic degradation performance

The photocatalytic degradation performance of the as-prepared samples were examined toward photodegradation of methyl orange (MO), bisphenol A (BPA) and 4-chlorophenol (4-CP) in aqueous solution under visible light irradiation ($\lambda > 420 \text{ nm}$, 300 W xenon lamp). Typically, 0.02 g as-prepared photocatalyst was added into an MO (80 mL, 10 mg L⁻¹) or BPA (80 mL, 10 mg L⁻¹) or 4-CP (80 mL, 10 mg L⁻¹) aqueous solution. The suspension were sonicated for 5 min to disperse the photocatalysts completely, followed by stirring under dark for 30 min to achieve the saturated adsorption. After that, the lamp was turned on and 4 mL aliquots were extracted from each sample at regular intervals and centrifuged to remove the catalysts. During the photoreactions, the experiment temperature was kept at 30 °C by using a circulating water system. And an air pump was employed to offer oxygen. The concentration of MO and 4-CP were analyzed on a UV-vis spectrophotometer (UV-2450, Shimadzu) at wavelength 463 nm and 225 nm, respectively. An Agilent TC-C18 column with two Varian ProStar 210 pumps and a Varian ProStar 325 UV-vis Detector was used to analyze the concentration of BPA at a wavelength of 230 nm. The mobile phase was 1 mL min⁻¹ with a solution of methanol and H₂O (v:v = 75: 25).

3. Results and discussion

3.1. The designation of $\text{Ag}_3\text{PO}_4@\text{CoFe}_2\text{O}_4$ nanostructures

Firstly, the phosphate salts were found to play the determining role in the formation of sesame ball like $\text{Ag}_3\text{PO}_4@\text{CoFe}_2\text{O}_4$ nanostructures. The typical TEM and SEM images of CoFe_2O_4 NPs are shown in Fig. S1a and Fig. S2a, respectively. The pure CoFe_2O_4 is spherical nanoparticles with a narrow particle size distribution of $12.0 \pm 2 \text{ nm}$ (Fig. S1b). Fig. S1c displayed the zeta potential of CoFe_2O_4 NPs with different pH values, it can be seen that the surface charge of CoFe_2O_4 NPs can be turned from positive to negative by changing the pH of the solution [43]. As shown in Scheme 1, if taking the NaH_2PO_4 as the PO_4^{3-} source, the surface charge of CoFe_2O_4 NPs will be positive. As a result, the positive poles of CoFe_2O_4 and Ag^+ will repel each other. Therefore, discussion about it is out of the present study. Fig. S2b and c displayed the Ag_3PO_4 and $\text{CoFe}_2\text{O}_4/\text{Ag}_3\text{PO}_4$ composites synthesized by using Na_2HPO_4 ,

respectively. It can be seen that the pure Ag_3PO_4 (Na_3PO_4) possess irregular spherical structures with a smooth surface, and the $\text{CoFe}_2\text{O}_4/\text{Ag}_3\text{PO}_4$ composite (Na_3PO_4) displayed a typical mixture morphology instead of composites morphology, in which the CoFe_2O_4 NPs were agglomerating and isolated. This can be explained by using Na_2HPO_4 as the PO_4^{3-} source, the surface charge of CoFe_2O_4 NPs wasn't negative enough to catch Ag^+ in the Ag_3PO_4 formation process. Consequently, the CoFe_2O_4 NPs and Ag_3PO_4 particles could not achieve a good combination. When the Na_3PO_4 was employed as the PO_4^{3-} source, because of the strong alkali property of Na_3PO_4 , the synthetic conditions for $\text{Ag}_3\text{PO}_4@\text{CoFe}_2\text{O}_4$ were in a high pH value and thus the surface charge of CoFe_2O_4 NPs will be turned negative enough to adsorb Ag^+ firmly. Finally, the CoFe_2O_4 NPs can attach on the surface of Ag_3PO_4 particles with the Ag^+ [44]. Fig. S2d shows the SEM image of pure Ag_3PO_4 (Na_3PO_4). It is clear that the pure Ag_3PO_4 synthesized via using Na_3PO_4 was consisted of irregular polyhedral crystal structures with a diameter of ca. 2 μm and some nanoparticles with a diameter of ca. 200 nm. After the CoFe_2O_4 NPs were introduced, the morphologies of Ag_3PO_4 (Na_3PO_4) were not changed obviously (as shown in Fig. S2e). From the high-powered scanning electron micrograph (Fig. S2f), it should be noticed that the surface of Ag_3PO_4 (Na_3PO_4) nanoparticles was inlaid with monodisperse CoFe_2O_4 NPs, which is a strong evidence for the formation of $\text{Ag}_3\text{PO}_4@\text{CoFe}_2\text{O}_4$ composites (Na_3PO_4).

Secondly, the hydrothermal treatment allows the above synthesized $\text{Ag}_3\text{PO}_4@\text{CoFe}_2\text{O}_4$ composites (Na_3PO_4) to form a uniform and highly crystallized sesame ball like $\text{Ag}_3\text{PO}_4@\text{CoFe}_2\text{O}_4$ composite, which is due to the regrowth of Ag_3PO_4 in the hydrothermal process [45]. As shown in Fig. 1a, after hydrothermal treatment, the pure Ag_3PO_4 (Na_3PO_4) has been turned from irregular polyhedral crystal and nanoparticle to regular spherical morphology at the size of 2–3 μm with a smooth surface (Fig. 1b and c). The $\text{Ag}_3\text{PO}_4@\text{CoFe}_2\text{O}_4$ composites (Na_3PO_4) exhibit the same results with that of pure Ag_3PO_4 (Na_3PO_4) after hydrothermal treatment. Uniform monodisperse $\text{Ag}_3\text{PO}_4@\text{CoFe}_2\text{O}_4$ particles can be observed in Fig. 1d. After amplifying the SEM image (Fig. 1e), it could be clearly seen that CoFe_2O_4 nanoparticles were evenly and tightly attached on the surface of Ag_3PO_4 , which was further verified by the TEM images (Fig. 1f). Moreover, the uniform distribution and tightly attaching of CoFe_2O_4 on the surface of Ag_3PO_4 particles ensure the as-prepared $\text{Ag}_3\text{PO}_4@\text{CoFe}_2\text{O}_4$ composite can be totally separated from solution by an extra magnetic field. At the meantime, EDS mapping was carried out to further reveal the distribution of the CoFe_2O_4 NPs, as shown in Fig. 1g, clearly demonstrate the homogeneously distribution of Ag (tangerine), P (green), O (red), Fe (yellow) and Co (blue). Hereto, the uniform monodisperse Ag_3PO_4 and $\text{Ag}_3\text{PO}_4@\text{CoFe}_2\text{O}_4$ particles have been successfully prepared, the following discussion are all about the uniform monodisperse Ag_3PO_4 and $\text{Ag}_3\text{PO}_4@\text{CoFe}_2\text{O}_4$ particles.

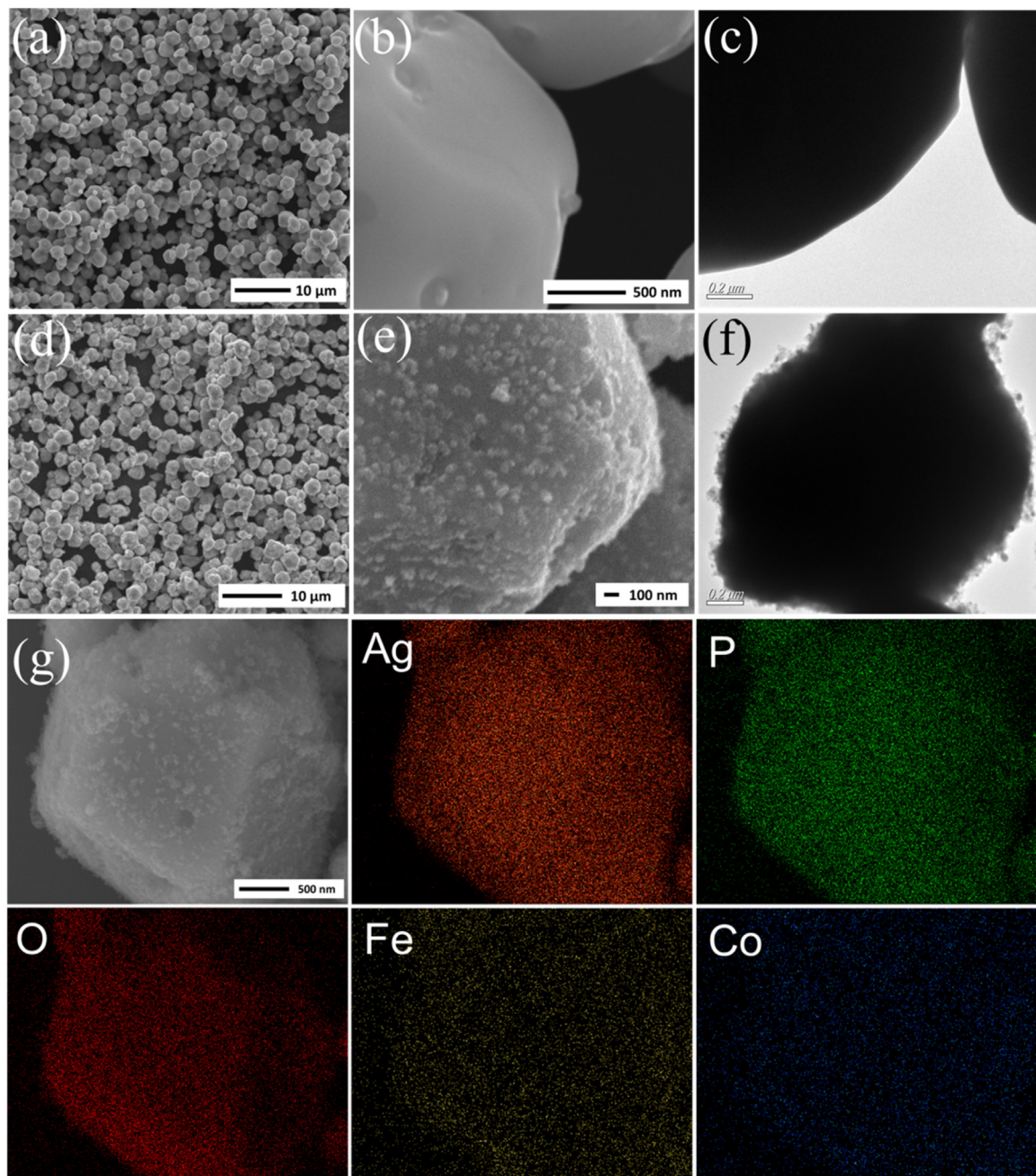


Fig. 1. SEM images of the as-prepared samples after hydrothermal treatment: (a and b) pure Ag_3PO_4 ; (d and e) $\text{Ag}_3\text{PO}_4@\text{CoFe}_2\text{O}_4$ composite; TEM images of (c) pure Ag_3PO_4 and (f) 3% $\text{Ag}_3\text{PO}_4@\text{CoFe}_2\text{O}_4$ composite; (g) EDS mappings of the 3% $\text{Ag}_3\text{PO}_4@\text{CoFe}_2\text{O}_4$ composite. (For interpretation of the references to colour in the text, the reader is referred to the web version of this article.)

3.2. Characterization of $\text{Ag}_3\text{PO}_4@\text{CoFe}_2\text{O}_4$ composites

X-ray diffraction (XRD) patterns of as-prepared Ag_3PO_4 , CoFe_2O_4 and $\text{Ag}_3\text{PO}_4@\text{CoFe}_2\text{O}_4$ composites are shown in Fig. 2. It can be seen that all the diffraction peaks of pure Ag_3PO_4 can be indexed to the body-centered cubic phase of Ag_3PO_4 (JCPDS No. 84-0510) and these peaks are strong and sharp, indicating that the as-prepared Ag_3PO_4 sample has a high crystallinity after hydrothermal treatment [45]. All the XRD patterns of $\text{Ag}_3\text{PO}_4@\text{CoFe}_2\text{O}_4$ composites are nearly identical to those of pure Ag_3PO_4 , suggesting that the loading of CoFe_2O_4 NPs didn't change the phase of Ag_3PO_4 or incorporated into the lattice of Ag_3PO_4 . For the XRD pattern of pure CoFe_2O_4 , the obvious peaks at $2\theta = 18.2^\circ, 30.1^\circ, 35.4^\circ, 43.5^\circ, 53.9^\circ, 57.1^\circ$ and 62.7° are matched with the plans of spinel-type

CoFe_2O_4 (JCPDS No. 22-1086). In addition, the peaks of CoFe_2O_4 are ambiguously observed in the $\text{Ag}_3\text{PO}_4@\text{CoFe}_2\text{O}_4$ composite materials, which should be ascribed to the high crystallinity diffraction peaks of Ag_3PO_4 and the content of CoFe_2O_4 is low in the hybrid system.

X-ray photoelectron spectroscopy (XPS) was used to further reveal the elemental composition and structure of the as-prepared samples. From the XPS survey spectra in Fig. S3, it can be seen that the Ag, P, O and C elements are contained in the pure Ag_3PO_4 and Ag, P, O, Co, Fe and C elements are observed in the 3% $\text{Ag}_3\text{PO}_4@\text{CoFe}_2\text{O}_4$ composite, which are in accord with the chemical constituent of the samples. In the high-resolution of Ag 3d spectra (Fig. 3a), the binding energies of Ag 3d_{5/2} and Ag 3d_{3/2} in the spectra of Ag_3PO_4 appear at 368.0 eV and 374.0 eV, respectively, and in

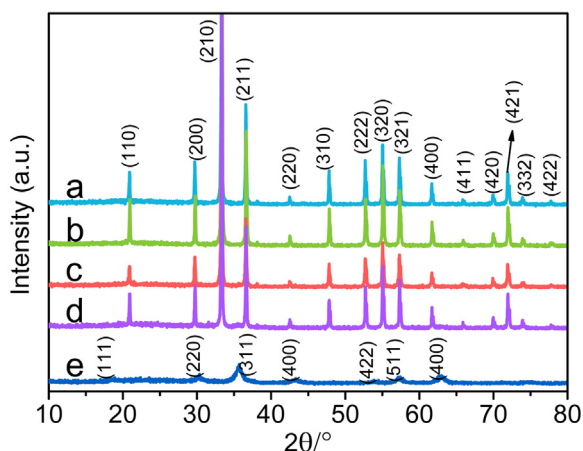


Fig. 2. XRD patterns of the as-prepared samples: (a) Ag_3PO_4 ; (b) 1% $\text{Ag}_3\text{PO}_4@\text{CoFe}_2\text{O}_4$; (c) 3% $\text{Ag}_3\text{PO}_4@\text{CoFe}_2\text{O}_4$; (d) 5% $\text{Ag}_3\text{PO}_4@\text{CoFe}_2\text{O}_4$; (e) CoFe_2O_4 .

the spectra of 3% $\text{Ag}_3\text{PO}_4@\text{CoFe}_2\text{O}_4$ composite are at 367.8 eV and 373.8 eV, respectively. Obviously, the Ag 3d spectra of 3% $\text{Ag}_3\text{PO}_4@\text{CoFe}_2\text{O}_4$ composite showed about 0.2 eV negative shifts in contrast to that of Ag_3PO_4 , suggesting that the chemical environment of Ag^+ have changed when Ag_3PO_4 coupled with CoFe_2O_4 . For the P 2p spectra (Fig. 3b), the peak binding energies are centered at 132.6 eV and 132.4 eV for Ag_3PO_4 and 3% $\text{Ag}_3\text{PO}_4@\text{CoFe}_2\text{O}_4$ composite, respectively. Similarly, 0.2 eV negative shifts have been observed in the spectra of 3% $\text{Ag}_3\text{PO}_4@\text{CoFe}_2\text{O}_4$ composite, indicating different chemical environment of P^{5+} in the Ag_3PO_4 and 3% $\text{Ag}_3\text{PO}_4@\text{CoFe}_2\text{O}_4$ composite. The negative shifts in the binding energy of Ag 3d and P 2p in the 3% $\text{Ag}_3\text{PO}_4@\text{CoFe}_2\text{O}_4$ composite might be attributed to the interaction of Ag^+ and P^{5+} ions with the CoFe_2O_4 nanoparticles, similar results have been observed in previous works [32,42]. In addition, it is worthwhile to note that the

intensity of Ag 3d and P 2p in the spectra of 3% $\text{Ag}_3\text{PO}_4@\text{CoFe}_2\text{O}_4$ composite is much lower than that of Ag_3PO_4 , respectively. Considering that the XPS signals were mainly collected from the surface of the sample with depth less than 10 nm, the decreased Ag 3d and P 2p spectra signals again verified the CoFe_2O_4 NPs were attached on the surface of Ag_3PO_4 [21]. Fig. 3c displayed the high-resolution of Co 2p spectra, there are two peaks appeared around 708.8 eV and 796.1 eV, which can be ascribed to the binding energies of Co 2p $3/2$ and Co 2p $1/2$, respectively. The bands of Fe 2p are shown in Fig. 3d, in which the peak at 711.5 eV is attributed to Fe 2p $3/2$ and the peak at 724.8 eV can be attributed to Fe 2p $1/2$ [38]. XPS results confirmed that the CoFe_2O_4 NPs were cover on the surface of Ag_3PO_4 again, which is consistent with the SEM analysis.

3.3. Magnetic properties

The magnetization curves were carried out to reveal the magnetic features of the as-prepared CoFe_2O_4 and 3% $\text{Ag}_3\text{PO}_4@\text{CoFe}_2\text{O}_4$ composites, which were measured under room temperature and the applied magnetic field was 20 kOe. As shown in Fig. 4, the magnetization curve of CoFe_2O_4 exhibits a feature of ferri-magnetic, of which the saturation magnetization (M_s), remnant magnetization (M_r) and coercivity (H_c) are 29.4 emu g $^{-1}$, of 2.3 emu g $^{-1}$ and 199.7 Oe, respectively. A similar magnetic behavior was observed for the 3% $\text{Ag}_3\text{PO}_4@\text{CoFe}_2\text{O}_4$ composite with saturation magnetization (M_s) of 1.8 emu g $^{-1}$, remnant magnetization (M_r) of 0.24 emu g $^{-1}$ and coercivity (H_c) of 199.7 Oe. The decreased saturation magnetization (M_s) and remnant magnetization (M_r) of 3% $\text{Ag}_3\text{PO}_4@\text{CoFe}_2\text{O}_4$ composite are due to the contribution of the non-magnetic Ag_3PO_4 to the total mass of the sample [46]. However, it should be noted that the coercivities (H_c) of the $\text{Ag}_3\text{PO}_4@\text{CoFe}_2\text{O}_4$ composite and CoFe_2O_4 NPs are all around 199.6 Oe without much difference as shown in the insert graph (bottom right corner). Suggesting that the magnetic properties of CoFe_2O_4 was not been changed in the synthesis process, which means the as-prepared 3%

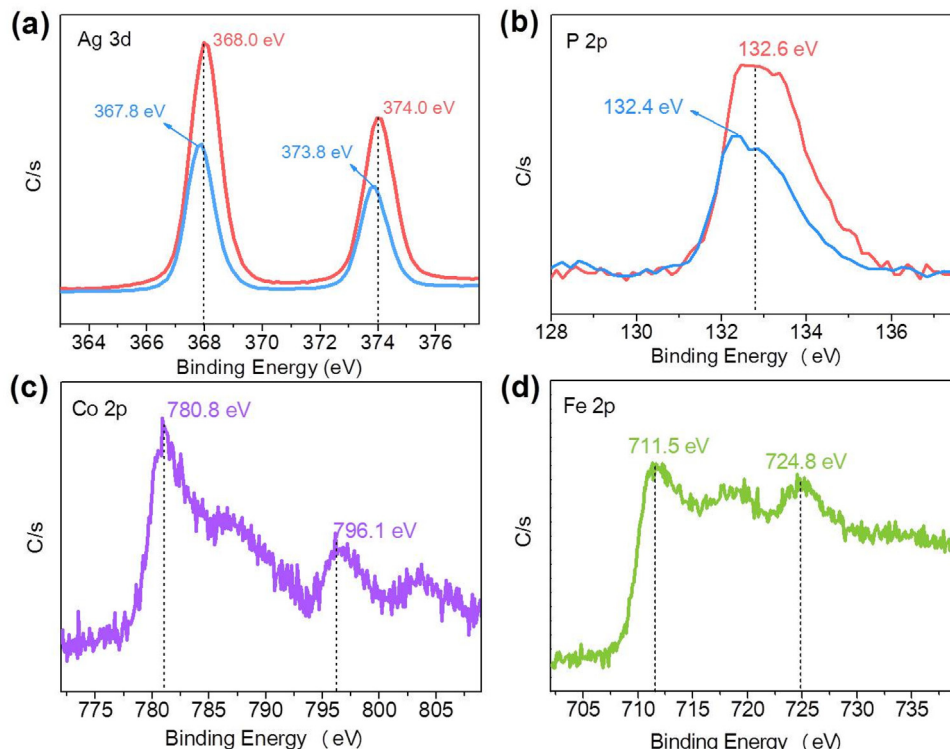


Fig. 3. XPS spectra of the as-prepared photocatalysts: (a) Ag 3d; (b) P 2p; (c) Co 2p; (d) Fe 2p.

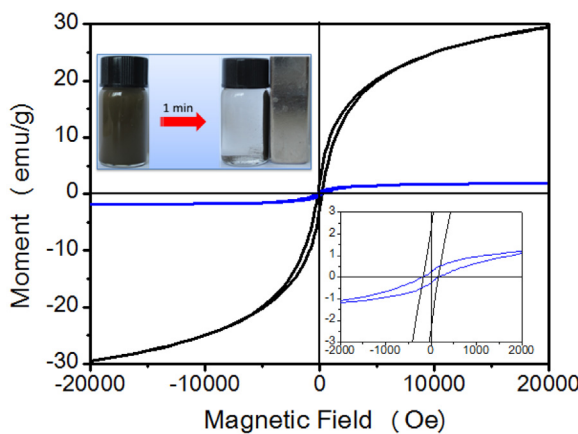


Fig. 4. Magnetization curves of the as-prepared CoFe_2O_4 and 3% $\text{Ag}_3\text{PO}_4@\text{CoFe}_2\text{O}_4$ composite (the inset graph shows the 3% $\text{Ag}_3\text{PO}_4@\text{CoFe}_2\text{O}_4$ composite sample dispersed in water (left) and separated by external magnet (right)).

$\text{Ag}_3\text{PO}_4@\text{CoFe}_2\text{O}_4$ composite photocatalysts could be collected by an extra magnetic field, as shown in the inset graph top left corner (without (left) and with a magnetic field (right)).

3.4. Photocatalytic disinfection

Despite Ag_3PO_4 has been recognized as a promising antibacterial agent utilized in the pharmaceutical field, the reports about photocatalytic antibacterial properties of Ag_3PO_4 are rare [47–50]. Here, *E. coli* was chosen as a model bacterium to evaluate the photocatalytic disinfection activity of the prepared photocatalysts. Fig. 5a displays the results of dark control experiments. It can be seen that the density of bacterial decreased about 1.0 log cfu/mL after 40 min in dark, suggesting low toxic effect over the present low concentration of Ag_3PO_4 . Besides, the CoFe_2O_4 NPs showed almost no toxic

effect against *E. coli* in dark. For the photocatalytic experiments (Fig. 5b), no bacterial inactivation was observed in light control (light irradiation without catalysts), indicating that only visible-light irradiation had no bactericidal effect on the bacterial cells. Meanwhile, in the present of photocatalysts, the remained bacterial population was decreased regularly over the pure CoFe_2O_4 , pure Ag_3PO_4 , 1% $\text{Ag}_3\text{PO}_4@\text{CoFe}_2\text{O}_4$, 3% $\text{Ag}_3\text{PO}_4@\text{CoFe}_2\text{O}_4$ and 5% $\text{Ag}_3\text{PO}_4@\text{CoFe}_2\text{O}_4$ with the cell density of $10^{6.69}$, $10^{3.33}$, $10^{2.01}$, 10^0 and $10^{1.39}$, respectively. It was clearly that the photocatalytic disinfection activity of Ag_3PO_4 was greatly enhanced by introducing CoFe_2O_4 . The optimum photocatalyst is 3% $\text{Ag}_3\text{PO}_4@\text{CoFe}_2\text{O}_4$, which means the proper decoration of CoFe_2O_4 NPs on the surface of Ag_3PO_4 plays an important role in the enhancement of photocatalytic disinfection efficiency. The possible interpretation for this tendency may be that excess CoFe_2O_4 NPs would shield Ag_3PO_4 particles from light harvesting, and result in the decreased photocatalytic disinfection activity.

Considering that the Ag^+ ions have been well documented with toxic effect towards multifaceted bactericidal substance. Actually, An and his groups have reported that the Ag based photocatalysts would release Ag^+ ions during light irradiation [51]. Therefore, the Ag^+ ions released in the photocatalysis process was studied. As shown in Fig. S4, the concentration of Ag^+ ions was found to be 0.2064–0.3027 $\mu\text{g}/\text{mL}$ in the photocatalytic process. According to the reports, Ag^+ ions almost have no bactericidal effect toward *E. coli* when the concentration is lower than 0.5 $\mu\text{g}/\text{mL}$ [52,53]. It indicated the Ag ions leaked from the as-prepared photocatalysts here have little contribution to the bactericidal effect of $\text{Ag}_3\text{PO}_4@\text{CoFe}_2\text{O}_4$. Thus, it suggests that the ROS generated during the photocatalytic process should be mainly responsible for the excellent bactericidal effect of composite photocatalysts. In order to reveal which species played the prominent role in the photocatalytic inactivation process, a series of ROS-scavenging experiments were conducted. The scavengers used in the photocatalytic disinfection experiments were:

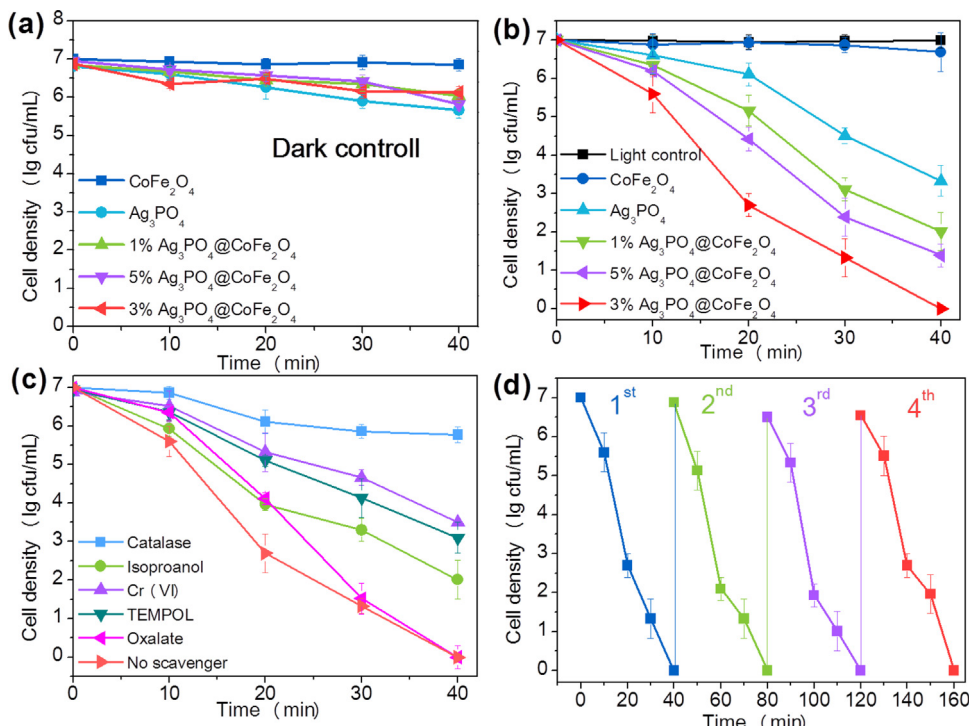


Fig. 5. (a) Inactivation of *E. coli* by the as-prepared samples in the dark. (b) Photocatalytic inactivation of *E. coli* by the as-prepared samples. (c) Photocatalytic disinfection performance with respective ROSs scavengers (Catalase, 0.4 mg/mL; isopropanol, 0.1 mM; Cr(VI), 0.01 mM; TEMPOL, 0.5 mM; sodium oxalate, 0.1 mM) in the presence of 3% $\text{Ag}_3\text{PO}_4@\text{CoFe}_2\text{O}_4$ composite. (d) Inactivation of *E. coli* by 3% $\text{Ag}_3\text{PO}_4@\text{CoFe}_2\text{O}_4$ composite in different repeated cycles.

catalase for the H_2O_2 [25], Cr(VI) for the photo-excited electrons, 4-hydroxy-2,2,6,6-tetramethyl-piperidinyloxy (TEMPO) for the $\text{O}_2^{\bullet-}$, isopropanol for the $\cdot\text{OH}$ and oxalate for the photo-excited holes [54]. The results are shown in Fig. 5c. Compared with that of no scavenger, the photocatalytic disinfection efficiency order is catalase < Cr(VI) < TEMPO < isopropanol < oxalate, which means that H_2O_2 causes the strongest effect in killing bacteria, and that oxygen related ROS dominates the disinfection effect. These results confirmed that the ROS were the main reason for the excellent bactericidal effect.

The stability and recyclability of photocatalysts is crucial for their practical applications in water treatment. Moreover, this is meaningful to design such a magnetic photocatalyst. Fig. 5d displays the recycle experiments, which was investigated by repeating photocatalytic disinfection experiment of *E. coli* with recycled 3% $\text{Ag}_3\text{PO}_4@\text{CoFe}_2\text{O}_4$ composite. The 3% $\text{Ag}_3\text{PO}_4@\text{CoFe}_2\text{O}_4$ composite photocatalyst was simply collected by a magnetmagnetic separation after each cycle and immediately used for the next bacterial inactivation cycle without any washing. It was clear that the 3% $\text{Ag}_3\text{PO}_4@\text{CoFe}_2\text{O}_4$ composite exhibited insignificant reduction in *E. coli* inactivation efficiency after four consecutive cycles. The result indicates the $\text{Ag}_3\text{PO}_4@\text{CoFe}_2\text{O}_4$ composites possess high stability and meet the concept of “green chemistry”. The TEM images of Ag_3PO_4 and 3% $\text{Ag}_3\text{PO}_4@\text{CoFe}_2\text{O}_4$ composite after photocatalytic disinfection reaction are displayed in Fig. 7, it can be seen that the surface of Ag_3PO_4 has changed to be rough rather than smooth (Fig. 7a) after photocatalytic reactions, suggesting serious photocorrosion of Ag_3PO_4 . As for the 3% $\text{Ag}_3\text{PO}_4@\text{CoFe}_2\text{O}_4$ composite, the CoFe_2O_4 NPs was still attached on the surface of Ag_3PO_4 (Fig. 7b), indicating the 3% $\text{Ag}_3\text{PO}_4@\text{CoFe}_2\text{O}_4$ composite possesses good structural stability.

3.5. Photocatalytic degradation of organic pollutants

The photodegradation of MO in the presence of as-prepared samples under visible-light irradiation was shown in Fig. 6a, in the blank curve, negligible degradation of MO can be observed, implying the MO is stable under visible light irradiation. After visible light irradiation for 30 min, only 64.2% MO was degraded by pure Ag_3PO_4 . When the Ag_3PO_4 was decorated with CoFe_2O_4 , the photocatalytic degradation efficiency of MO was greatly enhanced. The MO degradation efficiencies over 1%, 3% and 5% $\text{Ag}_3\text{PO}_4@\text{CoFe}_2\text{O}_4$ composite were 86.1%, 98.0% and 93.7%, respectively. Notably, the photocatalytic activity of $\text{Ag}_3\text{PO}_4@\text{CoFe}_2\text{O}_4$ composite was strengthened gradually with the CoFe_2O_4 content increasing from 1% to 3% hybrid material. However, a weakened photocatalytic activity was observed over the 5% hybrid material. A pseudo-first-order kinetic model was employed to fit the MO degradation data over different catalysts (Fig. S5a). And the apparent rate constant (k , min^{-1}) are displayed in Table S1. It can be found that the 3% $\text{Ag}_3\text{PO}_4@\text{CoFe}_2\text{O}_4$ composite has the highest photodegradation rate (about 0.12816 min^{-1}), which is 9.28 times higher than that of pure Ag_3PO_4 (0.01381 min^{-1}). The time-dependent absorption spectra of MO solution over 3% $\text{Ag}_3\text{PO}_4@\text{CoFe}_2\text{O}_4$ composite were carried out to investigate the variation of MO in the photocatalysis process. As shown in Fig. S5b, the maximal MO absorption at $\lambda = 463 \text{ nm}$ decreased gradually and no shift could be observed, indicating that the MO structure was destroyed directly. The inset graph in Fig. S5b shows the MO turned from yellow to colorless. In order to eliminate the photosensitization, the degradation of colorless BPA and 4-CP under visible light irradiation have also been carried out and the results are showed in Fig. S7.

To understand the roles of the active oxygen species on the photocatalysis organic pollutant degradation process over $\text{Ag}_3\text{PO}_4@\text{CoFe}_2\text{O}_4$ composite, the trapping experiments on the MO degradation were carried out. As shown in Fig. 6b, when tri-

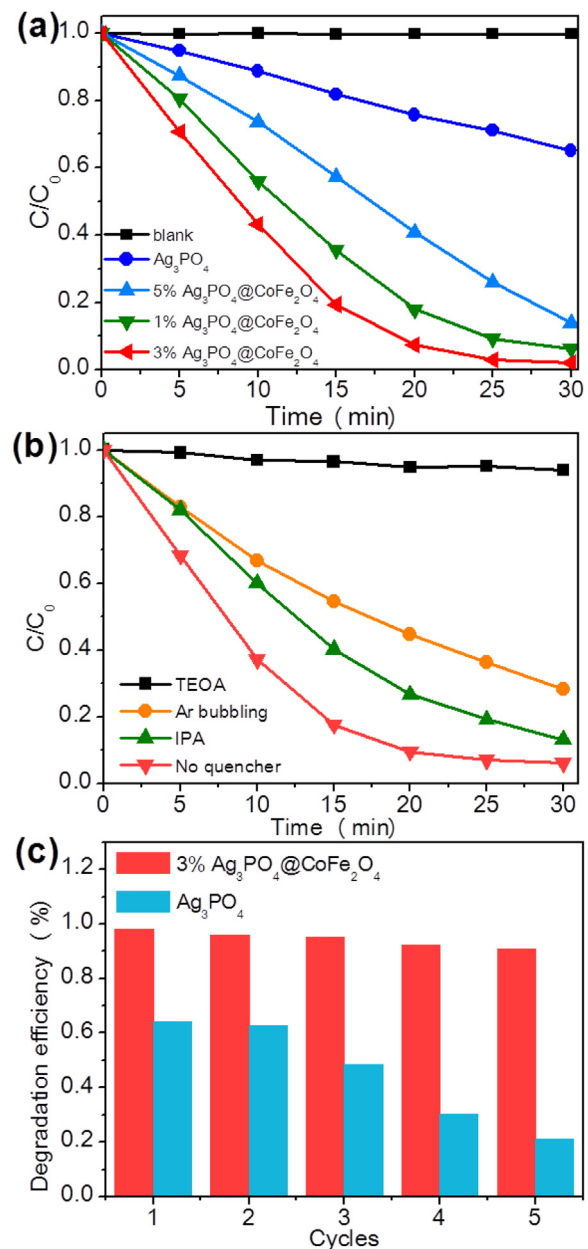


Fig. 6. (a) Photocatalytic degradation of MO by the as-prepared samples. (b) Trapping experiment of active species during the photocatalytic degradation of MO. (c) Recycling runs of the degradation of MO over Ag_3PO_4 and 3% $\text{Ag}_3\text{PO}_4@\text{CoFe}_2\text{O}_4$ composite.

ethanolamine (TEOA) was added, the degradation rate of MO was greatly inhibited, indicating the holes were the dominant reactive species. The degradation rate of MO decreased a lot under an Ar atmosphere. The most reasonable reason for this is that the decreased consumption of electrons by the O_2 on the CB edges of Ag_3PO_4 , because the electrons and holes are formed in a pair, their consumption should occur at the same time. Otherwise, the recombination of the electron-hole pairs would be happened, and the photocatalytic activity would decrease [55]. When the hydroxyl radical ($\cdot\text{OH}$) were scavenged by adding 2-propanol (IPA), the MO degradation rate was decreased, suggesting the hydroxyl radical ($\cdot\text{OH}$) played a role in the MO photocatalytic degradation process. The results of trapping experiments on the MO degradation indicate the holes govern the photocatalytic degradation activities.

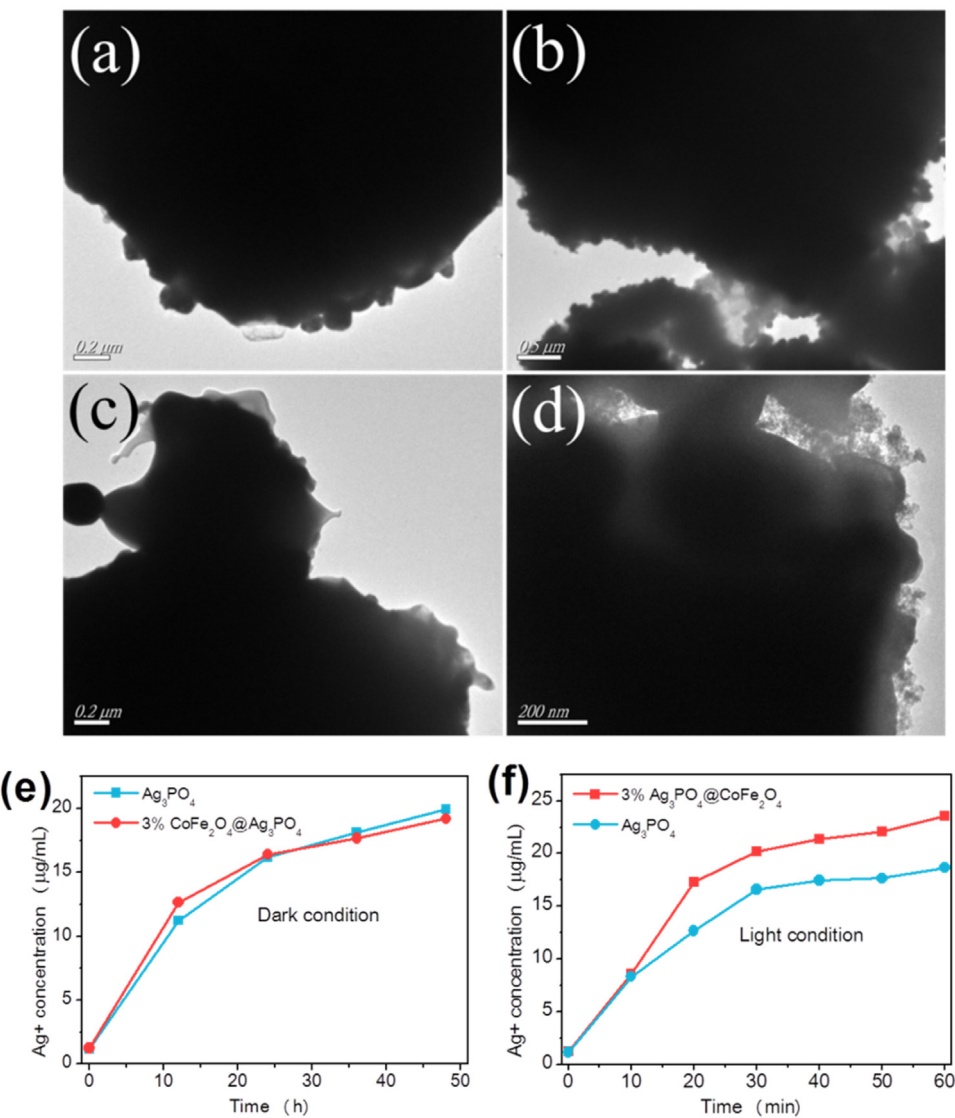


Fig. 7. TEM images of the as-prepared samples after photocatalytic disinfections: (a) Ag₃PO₄ and (b) 3% Ag₃PO₄@CoFe₂O₄ composites; TEM images of the as-prepared samples after photocatalytic degradation reactions: (c) Ag₃PO₄ and (b) 3% Ag₃PO₄@CoFe₂O₄ composites. The concentrations of Ag⁺ in the aqueous solution under (e) dark reaction conditions (f) light reaction conditions.

Fig. 6c displays the compared recycle runs of pure Ag₃PO₄ and 3% Ag₃PO₄@CoFe₂O₄ composite. Obviously, the degradation efficiency of pure Ag₃PO₄ drops from 64.2% to 9.8% after five recycles. It indicates the pure Ag₃PO₄ possesses poor stability under visible light irradiation, which is similar to the reported literatures [22,23]. The corresponding XRD patterns of the fresh Ag₃PO₄ and the used Ag₃PO₄ are displayed in Fig. S6a. Clearly, after photocatalytic reaction, the peaks of metallic Ag ($2\theta = 38.1^\circ$) appeared and the intensity was relative strong, which suggests a quick photoreduction has occurred on the bare Ag₃PO₄ in the photocatalytic process. On the contrary, in the recycle runs of 3% Ag₃PO₄@CoFe₂O₄ composite, the degradation efficiency can remain at 89.8% (the first cycle of 3% Ag₃PO₄@CoFe₂O₄ composite is 98.1%) after five consecutive recycles. Fig. S6b presents the XRD patterns of the fresh 3% Ag₃PO₄@CoFe₂O₄ and the used 3% Ag₃PO₄@CoFe₂O₄ composite. No evident changes can be found between the XRD patterns of the fresh and used samples, except for a very weak XRD peak of metallic Ag can be observed. It indicates the stability of Ag₃PO₄ has been remarkably improved in the Ag₃PO₄@CoFe₂O₄ composite. To gain more inside information about the enhanced stabilities of Ag₃PO₄@CoFe₂O₄ composite, the concentrations of Ag⁺ in the

aqueous solution under dark and photocatalytic reaction conditions have been analyzed, respectively [56]. In a typical procedure, 0.01 g of the as-prepared photocatalysts were dispersed in 40 mL deionized water and 5 mL aliquots were extracted from each sample at regular intervals to analyze the Ag⁺ concentrations by using ICP. The results are shown in Fig. 7e and f, it can be seen that the dissolutions of Ag₃PO₄ and 3% Ag₃PO₄@CoFe₂O₄ composite were almost the same in dark condition. While in the light condition, the 3% Ag₃PO₄@CoFe₂O₄ composite showed a higher dissolution feature than Ag₃PO₄, which can be explained by the CoFe₂O₄ NPs was mounted on the surface of Ag₃PO₄ particles and lead to more defects. However, from the results of the XRD patterns of used samples (Fig. S6), it is obvious that the reduction of Ag⁺ ions in Ag₃PO₄ to Ag metal has been inhibited in the Ag₃PO₄@CoFe₂O₄ composites. Therefore, there should be other reasons improved the stability. In order to further reveal these reasons, the TEM images of Ag₃PO₄ and 3% Ag₃PO₄@CoFe₂O₄ composite after photocatalytic degradation reactions also have been carried out. As shown in Fig. 7c, it can be seen that the morphologies of Ag₃PO₄ have been greatly changed, indicating the unstable abilities of Ag₃PO₄ in the photocatalytic degradation reactions process. For the 3% Ag₃PO₄@CoFe₂O₄ com-

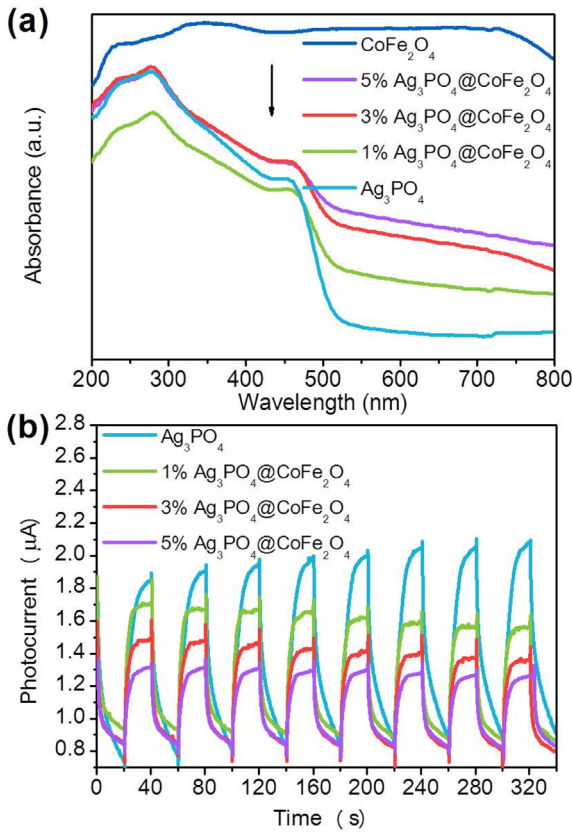


Fig. 8. (a) UV-vis diffuse reflectance spectra of the as-prepared samples; (b) Transient photocurrent responses of the as-prepared samples.

posite, it is clear that the CoFe₂O₄ NPs did not drop off (Fig. 7d). In Tang's review [57], he has declared that the bare Ag₃PO₄ suffered from photoreduction mainly because the photogenerated electrons on the CB of Ag₃PO₄ can reduce Ag⁺ ions in Ag₃PO₄ to Ag metal, and if photogenerated electrons are transferred or reduce O₂ (ORR) instead of reducing Ag⁺ ions in Ag₃PO₄ to Ag metal, the photoreduction of Ag₃PO₄ can be slowed down. Therefore, it can be speculated that the electrons should be more easily be consumed on the CB of Ag₃PO₄ in the Ag₃PO₄@CoFe₂O₄ composites and thus greatly improved the stability of Ag₃PO₄.

3.6. The role of CoFe₂O₄ in the Ag₃PO₄@CoFe₂O₄ composites

Normally, there are three critical properties governing the photocatalytic performance: (1) the light harvesting property, (2) the electron-hole pair's separation efficiency and (3) the utilization of electron-hole for the ROS production [58]. For the first one, the optical absorption properties, a broad light harvesting ability may result in generating more photo-excited electron-hole pairs and beneficial for the photocatalytic activity. Fig. 8a displays the DRS of the pure Ag₃PO₄, pure CoFe₂O₄ and Ag₃PO₄@CoFe₂O₄ composites with different CoFe₂O₄ content, which was employed to reveal the optical absorption properties of the as-prepared samples. The typical UV-vis spectra of pure Ag₃PO₄ showed an absorption region ranging from 200 nm to 530 nm, this originates from the intrinsic charge transfer response of Ag₃PO₄ from the valence band to the conduction band [10]. The pure CoFe₂O₄ exhibited a wide and strong absorption region ranging from 200 nm to 800 nm, this may mainly because of the nature color of CoFe₂O₄ is dark brown. When the Ag₃PO₄ was modified with CoFe₂O₄, no obviously absorption edge shifts can be found compared with that of Ag₃PO₄, whereas the light absorptions of Ag₃PO₄@CoFe₂O₄ composites in the region

of 530–800 nm have increased gradually from 1% to 5%. Indicating the loading of CoFe₂O₄ could optimize the absorption ability of Ag₃PO₄@CoFe₂O₄ composite.

For the second one, the separation efficiency always can be reflected by the measurements of photocurrent-time response and electrochemical impedance spectroscopy. The photocurrent-time response signals under visible light are displayed in Fig. 8b. It can be seen that after the CoFe₂O₄ NPs were added, the photocurrent response signals were decreased successively rather than enhanced. Meanwhile, the electrochemical impedance spectroscopy showed the same results. As shown in Fig. S8, the charge transfer efficiencies have been impaired apparently when the CoFe₂O₄ NPs were introduced.

For the third one, the ROS generation, most semiconductor materials are nonspecific in catalyzing ROS production. Therefore, materials with specific in catalyzing ROS production need to be combined in photocatalysis systems to further promote the photocatalytic activity [25]. Fig. 9a shows the polarization curves for the ORR. The average electron number calculated from the corresponding slope of Koutecky-Levich plots is 1.6 (Fig. 9b), indicating the two-electron oxygen reduction reaction for H₂O₂ generation was preferentially catalyzed over a four-electron transfer reaction on the as-prepared CoFe₂O₄ NPs. These results are agreeing with that CoFe₂O₄ NPs possess high peroxide species (HO₂⁻) yield property in the ORR process from the reports [59,60]. Therefore, the adding of CoFe₂O₄ NPs into Ag₃PO₄ photocatalysis would enhance the ROS generation. To prove evidence for this, ESR spin-trap spectra were carried out for the O₂^{•-} and •OH detection, and the H₂O₂ yield were determined by using colorimetric N,N-diethyl-p-phenylenediamine (DPD) method [61]. As shown in Fig. 9c and d. In the dark, there were no signals can be observed, indicating the formation of O₂^{•-} and •OH on the as-prepared samples needs light-irradiation. When the light was on, the characteristic peaks of DMPO-O₂^{•-} adduct (Fig. 9c) and DMPO-•OH adduct (Fig. 9d) have been observed both on pure Ag₃PO₄ and 3% Ag₃PO₄@CoFe₂O₄ composite photocatalysts. Moreover, it is obviously that both the DMPO-O₂^{•-} and DMPO-•OH signal intensity of the 3% Ag₃PO₄@CoFe₂O₄ composite is much higher than that of Ag₃PO₄, respectively. These results reveal that the introduction of CoFe₂O₄ NPs could enhance the formation of O₂^{•-} and •OH species. As for the H₂O₂ generation measurement (Fig. 9e), it is clear that the H₂O₂ yield was enhanced over the 3% Ag₃PO₄@CoFe₂O₄ composite, indicating that the modification of CoFe₂O₄ indeed benefit to the O₂ reduce to the H₂O₂. Considering that the surface area is also one of the crucial facts of the ROS generation efficiency due to larger surface area could offer more active sites for oxygen reduction reaction. In this study, the compared N₂ adsorption-desorption isotherm of Ag₃PO₄ and 3% Ag₃PO₄@CoFe₂O₄ composite were carried out. As shown in Fig. 9f, in which exhibit type IV isotherm with H3-type hysteresis loops. The Brunauer–Emmett–Teller (BET) specific surface area of Ag₃PO₄ and 3% Ag₃PO₄@CoFe₂O₄ composite were calculated to be 3.5042 m²/g and 3.8217 m²/g, respectively. It can be seen that the surface area did not increase evidently after Ag₃PO₄ particles modified with CoFe₂O₄ NPs, which means the enhanced surface area is not the main reason for increasing surface/interface catalytic reaction efficiency of this present photocatalysis system.

3.7. Photocatalytic enhancement mechanisms propose

According to all above-mentioned results and discussions, the appearance of photocurrent-time response decreasing and electrochemical impedance increasing can be explained as follows: In the Ag₃PO₄@CoFe₂O₄ composites system, the Ag₃PO₄ particles were covered by the CoFe₂O₄ NPs. When the Ag₃PO₄@CoFe₂O₄ composites were dropped onto the ITO glass, the poor electrical conductive

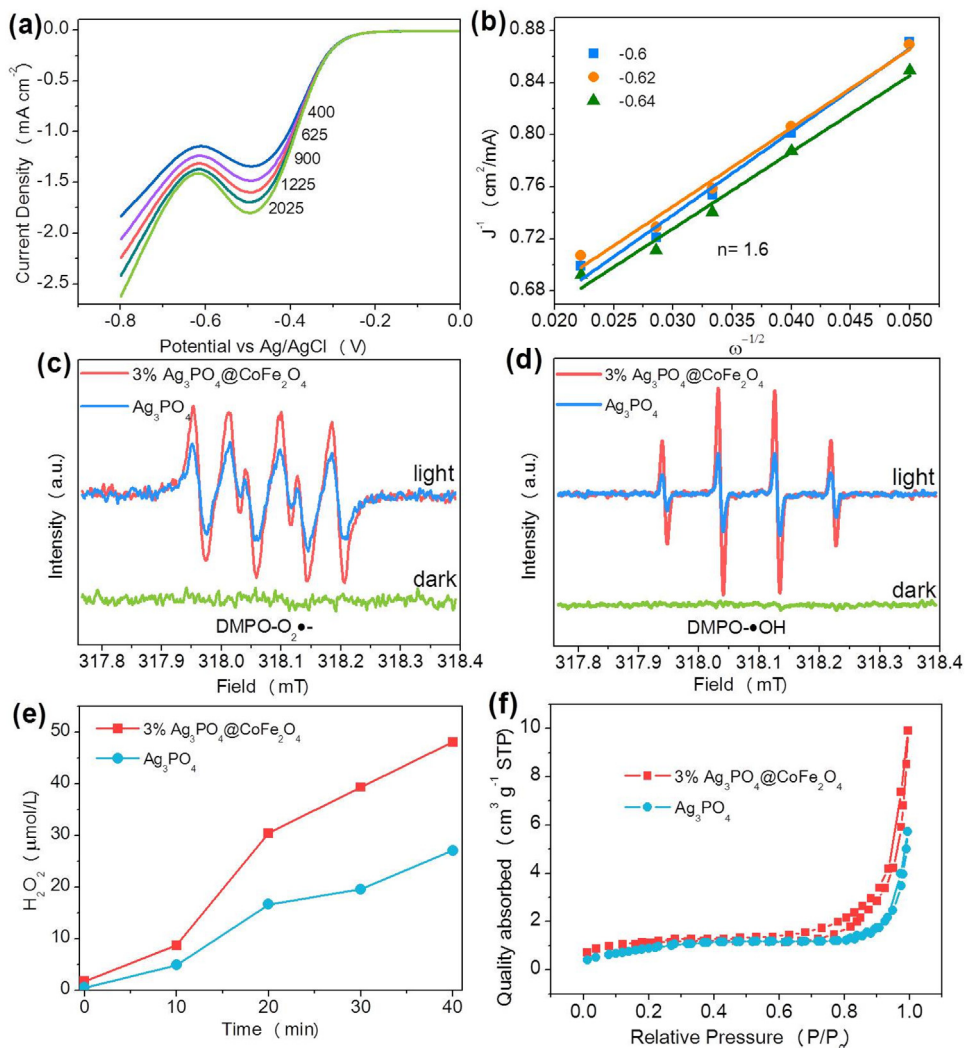


Fig. 9. (a) The polarization curves for the ORR on CoFe₂O₄ at a rotating speed of 400, 625, 900, 1225 and 2025 rpm. (b) The corresponding Koutecky-Levich plots. (c) ESR spectra of Ag₃PO₄/DMPO-OH and 3% Ag₃PO₄@CoFe₂O₄/DMPO-OH. (d) ESR spectra of Ag₃PO₄/DMPO-O₂^{•-} and 3% Ag₃PO₄@CoFe₂O₄/DMPO-O₂^{•-}. (e) Comparison of the H₂O₂ production on pure Ag₃PO₄ and 3% Ag₃PO₄@CoFe₂O₄ composite. (f) Nitrogen adsorption–desorption isotherm of as-prepared Ag₃PO₄ and 3% Ag₃PO₄@CoFe₂O₄ composite.

CoFe₂O₄ NPs were inserted between the Ag₃PO₄ and ITO glass [62]. Therefore, the photo-excited electrons were not easy to transfer to the ITO and a decreased photocurrent as well as high resistance were observed on the Ag₃PO₄@CoFe₂O₄ composites, which seems reduced the electron-hole separation efficiency. However, according to the photocatalytic activities test and ESR, H₂O₂ yield test, the photocatalytic performance of Ag₃PO₄@CoFe₂O₄ composites and the ROS generation efficiencies indeed enhanced, which means the electrons consumption efficiencies were increased and the electron-hole pair separation efficiencies were improved. To proof this assumption, we designed an O₂ control photocurrent experiments as follows: the 3% Ag₃PO₄@CoFe₂O₄ modified ITO working electrodes and PBS electrolyte were kept at flowing N₂ ambient for 1 h prior to the measurements to eliminate the adsorbed and dissolved O₂. Subsequently, the N₂ pretreatment working electrodes were inserted in a quartz cell filled with N₂ pretreatment 0.1 M PBS electrolyte and collected the photocurrent signals. After several steady turn-off cycles, paused the measurement and O₂ was slowly bubbled into the quartz cell for another 1 h. After that, restarting to collect the photocurrents signals. The results are displayed in Fig. 10a, it can be seen that the photocurrents intensity of 3% Ag₃PO₄@CoFe₂O₄ in O₂ was immediately decreased. These

results indicated that the photo-excited electrons by the Ag₃PO₄ were apt to react with the adsorbed O₂ instead of transfer to CoFe₂O₄ NPs due to the poor electrical conductivity features of pure CoFe₂O₄. O₂-TPD tests were performed on Ag₃PO₄ and 3% Ag₃PO₄@CoFe₂O₄ composites to characterize the O₂ adsorption abilities (Fig. S11a), and the TG measurements were carried out (Fig. S11b) [63]. Usually, the low-temperature desorption peak can be assigned to surface adsorption oxygen [64]. From Fig. S11a, it can be seen that compare to the pure Ag₃PO₄, the 3% Ag₃PO₄@CoFe₂O₄ exhibited an enhance O₂ desorption abilities below 200 °C, indicating that CoFe₂O₄ addition enhanced the adsorption of O₂ over the 3% Ag₃PO₄@CoFe₂O₄ catalyst [65,66]. The enhanced adsorption of O₂ by CoFe₂O₄ addition should also contribute to the excellent activity of 3% Ag₃PO₄@CoFe₂O₄ photocatalyst.

At last, we conducted the PL emission spectra to reveal the electron-hole pairs separation efficiencies, the results are showed in Fig. 10b, compared with the pure Ag₃PO₄, the PL intensity of 3% Ag₃PO₄@CoFe₂O₄ composite decreased to a certain extent, whereas the 3% Ag₃PO₄@CoFe₂O₄ composite exhibited quenched PL. The decreased PL intensity can be explained by the introduction of CoFe₂O₄ increased the O₂ adsorption/activation and accelerated the photo-excited electrons consumptions. Therefore, the charge

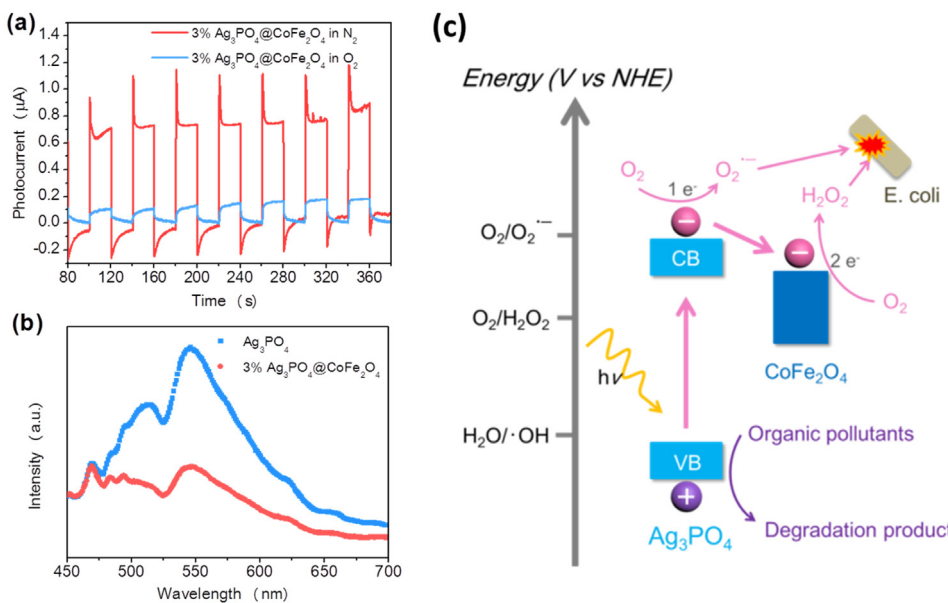


Fig. 10. (a) The O_2 control photocurrents signal of 3% Ag_3PO_4 @ CoFe_2O_4 composite; (b) Compared PL spectra of the pure Ag_3PO_4 and 3% Ag_3PO_4 @ CoFe_2O_4 composite; (c) Proposed mechanism of O-related radicals' generation in photocatalytic systems.

recombination on the Ag_3PO_4 surface was suppressed. In summary, the donate CoFe_2O_4 NPs on the surface of Ag_3PO_4 approach although apparently decreased the photocurrents and increased the resistance, in fact the O_2 adsorption and activation features of CoFe_2O_4 could enhance the electrons consumption and improve the electron-hole pairs separation efficiencies.

Upon elucidating the reaction process, we conclude that the surface modification of CoFe_2O_4 NPs could facilitate the O_2 adsorption and O–O bond activation/cleavage/oxide removal and accelerated two-electron oxygen reduction reaction for H_2O_2 generation on the surface of Ag_3PO_4 , thus enhanced the surface/interface catalytic reaction efficiency, which should be the dominating reason for Ag_3PO_4 @ CoFe_2O_4 composite exhibit enhanced photocatalytic performance. The mechanistic pathway as illustrated in Fig. 10c. Under visible-light illumination, the Ag_3PO_4 of the Ag_3PO_4 @ CoFe_2O_4 composites were photo-excited and produced electron-hole pairs. Note that, according to the DRS results the band gap of CoFe_2O_4 is as narrow as 0.8 eV (Fig. S9a), which means that the CoFe_2O_4 possess very high electron–hole recombination efficiency. Hence, it is considered that the photo-excited electron and holes on the CoFe_2O_4 are hardly participating in the present photocatalytic reaction. Normally, only few of the photo-generated electrons by the Ag_3PO_4 could react with the dissolved oxygen because of the difficulty in O_2 adsorption and O–O bond activation/cleavage/oxide removal. Therefore, these unreacted electrons are easily recombining with holes or reducing the Ag^+ in Ag_3PO_4 , thus decrease the photocatalytic activity and stability of Ag_3PO_4 . However, when the CoFe_2O_4 NPs were grafted on the surface of Ag_3PO_4 , because of the oxygen activation features (such as O_2 adsorption and O–O bond activation/cleavage/oxide removal) of CoFe_2O_4 NPs, the oxygen reduction reaction on Ag_3PO_4 's surface would be improved thus enhanced the electrons consume for ROS production, which play a key role in the water disinfection, and leave more holes for organic pollutants oxidation as well as increase the stability of Ag_3PO_4 .

4. Conclusions

In summary, we report a novel tactful strategy for evenly decorating CoFe_2O_4 NPs on the surface of Ag_3PO_4 particles. As a result, a magnetic Ag_3PO_4 @ CoFe_2O_4 composite photocatalyst

with uniform and highly crystallized sesame ball like structure was successfully synthesized. The as-prepared Ag_3PO_4 @ CoFe_2O_4 composite showed the simultaneous superior photocatalytic activities of water disinfection and organic degradation compared with Ag_3PO_4 . The enhanced photocatalytic performance is originated from the CoFe_2O_4 NPs possess specific catalyzing properties, which on the one hand can effectively catalyze the adsorbed O_2 into H_2O_2 on the surface of Ag_3PO_4 @ CoFe_2O_4 composite, thus greatly enhanced the water disinfection performance. On the other hand, the efficient consume of photo-excited electrons on the CB of Ag_3PO_4 not only leave more holes for organic pollutants degradation but also slow down the reduction of Ag^+ ions in Ag_3PO_4 to Ag metal and improved the stability of Ag_3PO_4 . As a result, the approach has efficiently enhanced the photocatalytic performance and stability of Ag_3PO_4 . This work thus clearly demonstrates that the surface catalysis engineering can serve as a versatile approach to refine catalysts, in efforts to promote the production of ROS and develop high efficient photocatalysts. The concept demonstrated here mainly highlights the importance of catalytic reaction step on the surface of a semiconductor in the whole photocatalysis process as well as structures versatile photocatalysts with wide application.

Acknowledgements

This work is financially supported by the National Natural Science Foundation of China for Youths (No. 21407065), Natural Science Foundation of Jiangsu Province for Youths (BK20140533), China Postdoctoral Science Foundation (2015T80514, 2016M591777). A Project Funded by the Priority Academic Program Development of Jiangsu Higher Education.

Appendix A. Supplementary data

Supplementary data associated with this article can be found, in the online version, at <http://dx.doi.org/10.1016/j.apcatb.2017.06.030>.

References

- [1] W.J. Ong, L.L. Tan, Y.H. Ng, S.T. Yong, S.P. Chai, Chem. Rev. 116 (2016) 7159–7329.

- [2] R.P. Schwarzenbach, B.I. Escher, K. Fenner, T.B. Hofstetter, C.A. Johnson, U.v. Gunten, B. Wehrli, *Science* 313 (2006) 1072–1077.
- [3] S. Ghosh, N.A. Kouame, L. Ramos, S. Remita, A. Dazzi, A. Deniset-Besseau, P. Beaunier, F. Goubard, P.H. Aubert, H. Remita, *Nat. Mater.* 14 (2015) 505–511.
- [4] D. Fattakhova-Rohlfing, A. Zaleska, T. Bein, *Chem. Rev.* 114 (2014) 9487–9558.
- [5] S. Gligorovski, R. Strekowski, S. Barbat, D. Vione, *Chem. Rev.* 115 (2015) 13051–13092.
- [6] M. Hayyan, M.A. Hashim, I.M. AlNashef, *Chem. Rev.* 116 (2016) 3029–3085.
- [7] H. Sun, G. Li, X. Nie, H. Shi, P.K. Wong, H. Zhao, T. An, *Environ. Sci. Technol.* 48 (2014) 9412–9419.
- [8] S. Loeb, R. Hofmann, J.-H. Kim, *Environ. Sci. Tech. Lett.* 3 (2016) 73–80.
- [9] D. Wang, D. Astruc, *Chem. Rev.* 114 (2014) 6949–6985.
- [10] Z. Yi, J. Ye, N. Kikugawa, T. Kako, S. Ouyang, H. Stuart-Williams, H. Yang, J. Cao, W. Luo, Z. Li, Y. Liu, R.L. Withers, *Nat. Mater.* 9 (2010) 559–564.
- [11] C. Cui, S. Li, Y. Qiu, H. Hu, X. Li, C. Li, J. Gao, W. Tang, *Appl. Catal. B Environ.* 200 (2017) 666–672.
- [12] X. Guan, L. Guo, *ACS Catal.* 4 (2014) 3020–3026.
- [13] Y. He, L. Zhang, B. Teng, M. Fan, *Environ. Sci. Technol.* 49 (2015) 649–656.
- [14] Y. Bi, S. Ouyang, N. Umezawa, J. Cao, J. Ye, *J. Am. Chem. Soc.* 133 (2011) 6490–6492.
- [15] B. Zheng, X. Wang, C. Liu, K. Tan, Z. Xie, L. Zheng, *J. Mater. Chem. A* 1 (2013) 12635.
- [16] T. Yan, W. Guan, J. Tian, P. Wang, W. Li, J. You, B. Huang, *J. Alloy. Compd.* 680 (2016) 436–445.
- [17] P. Amornpitoksuk, K. Intarasuwan, S. Suwanboon, J. Baltrusaitis, *Ind. Eng. Chem. Res.* 52 (2013) 17369–17375.
- [18] H. Yu, G. Cao, F. Chen, X. Wang, J. Yu, M. Lei, *Appl. Catal. B: Environ.* 160–161 (2014) 658–665.
- [19] T. Yan, J. Tian, W. Guan, Z. Qiao, W. Li, J. You, B. Huang, *Appl. Catal. B Environ.* 202 (2017) 84–94.
- [20] C. Tang, E. Liu, J. Wan, X. Hu, J. Fan, *Appl. Catal. B Environ.* 181 (2016) 707–715.
- [21] X. Yang, H. Cui, Y. Li, J. Qin, R. Zhang, H. Tang, *ACS Catal.* 3 (2013) 363–369.
- [22] Z.-M. Yang, G.-F. Huang, W.-Q. Huang, J.-M. Wei, X.-G. Yan, Y.-Y. Liu, C. Jiao, Z. Wan, A. Pan, *J. Mater. Chem. A* 2 (2014) 1750–1756.
- [23] L. Liu, Y. Qi, J. Lu, S. Lin, W. An, Y. Liang, W. Cui, *Appl. Catal. B Environ.* 183 (2016) 133–141.
- [24] H. Hussain, G. Tocci, T. Woolcot, X. Torrelles, C.L. Pang, D.S. Humphrey, C.M. Yim, D.C. Grinter, G. Cabailh, O. Bikondoa, R. Lindsay, J. Zegenhagen, A. Michaelides, G. Thornton, *Nat. Mater.* 16 (2017) 461–466.
- [25] C. Liu, D. Kong, P.C. Hsu, H. Yuan, H.W. Lee, Y. Liu, H. Wang, S. Wang, K. Yan, D. Lin, P.A. Maraccini, K.M. Parker, A.B. Boehm, Y. Cui, *Nat. Nanotechnol.* 11 (2016) 1098–1104.
- [26] G. Muscas, G. Singh, W.R. Glomm, R. Mathieu, P.A. Kumar, G. Concas, E. Agostinelli, D. Peddis, *Chem. Mater.* 27 (2015) 1982–1990.
- [27] A. López-Ortega, E. Lottini, C.d.J. Fernández, C. Sangregorio, *Chem. Mater.* 27 (2015) 4048–4056.
- [28] Y. Shi, K. Zhou, B. Wang, S. Jiang, X. Qian, Z. Gui, R.K.K. Yuen, Y. Hu, *J. Mater. Chem. A* 2 (2014) 535–544.
- [29] Y. Fu, H. Chen, X. Sun, X. Wang, *Appl. Catal. B Environ.* 111–112 (2012) 280–287.
- [30] M. Wang, Y.Q. Ma, X. Sun, B.Q. Geng, M.Z. Wu, G.H. Zheng, Z.X. Dai, *Appl. Surf. Sci.* 392 (2017) 1078–1087.
- [31] S. Ma, S. Zhan, Y. Jia, Q. Zhou, *ACS Appl. Mater. Inter.* 7 (2015) 10576–10586.
- [32] Y. Xu, T. Zhou, S. Huang, M. Xie, H. Li, H. Xu, J. Xia, H. Li, *RSC Adv.* 5 (2015) 41475–41483.
- [33] S. Huang, Y. Xu, M. Xie, H. Xu, M. He, J. Xia, L. Huang, H. Li, *Colloids Surf. A: Physicochem. Eng. Aspects* 478 (2015) 71–80.
- [34] L. Jing, Y. Xu, S. Huang, M. Xie, M. He, H. Xu, H. Li, Q. Zhang, *Appl. Catal. B Environ.* 199 (2016) 11–22.
- [35] S. Li, B. Wang, J. Liu, M. Yu, *Electrochim. Acta* 129 (2014) 33–39.
- [36] D. Tang, R. Yuan, Y. Chai, H. An, *Adv. Funct. Mater.* 17 (2007) 976–982.
- [37] L. Lu, Q. Hao, W. Lei, X. Xia, P. Liu, D. Sun, X. Wang, X. Yang, *Small* 11 (2015) 5833–5843.
- [38] A. Indra, P.W. Menezes, N.R. Sahraie, A. Bergmann, C. Das, M. Tallarida, D. Schmeisser, P. Strasser, M. Driess, *J. Am. Chem. Soc.* 136 (2014) 17530–17536.
- [39] H. Zhu, S. Zhang, Y.X. Huang, L. Wu, S. Sun, *Nano. Lett.* 13 (2013) 2947–2951.
- [40] L. Gan, L. Xu, K. Qian, *Mater. Design* 109 (2016) 354–360.
- [41] T. An, H. Sun, G. Li, H. Zhao, P.K. Wong, *Appl. Catal. B Environ.* 188 (2016) 360–366.
- [42] S. Huang, Y. Xu, Z. Chen, M. Xie, H. Xu, M. He, H. Li, Q. Zhang, *RSC Adv.* 5 (2015) 71035–71045.
- [43] S. Nappini, E. Magnano, F. Bondino, I. Píš, A. Barla, E. Fantechi, F. Pineider, C. Sangregorio, L. Vaccari, L. Venturelli, P. Baglioni, *J. Phys. Chem. C* 119 (2015) 25529–25541.
- [44] J. Guo, S. Ouyang, H. Zhou, T. Kako, J. Ye, *J. Phys. Chem. C* 117 (2013) 17716–17724.
- [45] X. Guan, J. Shi, L. Guo, *Int. J. Hydrogen Energ.* 38 (2013) 11870–11877.
- [46] C. An, X. Ming, J. Wang, S. Wang, *J. Mater. Chem.* 22 (2012) 5171.
- [47] J.J. Buckley, A.F. Lee, L. Olivé, K. Wilson, *J. Mater. Chem.* 20 (2010) 8056.
- [48] X. Yang, J. Qin, Y. Jiang, R. Li, Y. Li, H. Tang, *RSC Adv.* 4 (2014) 18627.
- [49] Q. Zhu, X. Hu, M.S. Stanislaus, N. Zhang, R. Xiao, N. Liu, Y. Yang, *Sci. Total. Environ.* 577 (2017) 236–244.
- [50] N.K. Eswar, P.C. Ramamurthy, G. Madras, *Photochem. Photobiol. Sci.* 14 (2015) 1227–1237.
- [51] D. Xia, T. An, G. Li, W. Wang, H. Zhao, P.K. Wong, *Water Res.* 99 (2016) 149–161.
- [52] S. Ma, S. Zhan, Y. Jia, Q. Shi, Q. Zhou, *Appl. Catal. B Environ.* 186 (2016) 77–87.
- [53] S. Pal, Y.K. Tak, J.M. Song, *Appl. Environ. Microbiol.* 73 (2007) 1712–1720.
- [54] T.W. Ng, L. Zhang, J. Liu, G. Huang, W. Wang, P.K. Wong, *Water Res.* 90 (2016) 111–118.
- [55] J. Sheng, X. Li, Y. Xu, *ACS Catal.* 4 (2014) 732–737.
- [56] L. Liu, L. Ding, Y. Liu, W. An, S. Lin, Y. Liang, W. Cui, *Appl. Catal. B Environ.* 201 (2017) 92–104.
- [57] D.J. Martin, G. Liu, S.J. Moniz, Y. Bi, A.M. Beale, J. Ye, J. Tang, *Chem. Soc. Rev.* 44 (2015) 7808–7828.
- [58] J. Yang, D. Wang, H. Han, C. Li, *Acc. Chem. Res.* 46 (2013) 1900–1909.
- [59] S. Liu, W. Yan, X. Cao, Z. Zhou, R. Yang, *Int. J. Hydrogen Energ.* 41 (2016) 5351–5360.
- [60] W. Bian, Z. Yang, P. Strasser, R. Yang, *J. Power Sources* 250 (2014) 196–203.
- [61] H. Bader, V. Sturzenegger, J. Hoigni, *Water Res.* 22 (1986) 1109–1111.
- [62] D. Chen, C. Chen, Z.M. Baiyee, Z. Shao, F. Ciucci, *Chem. Rev.* 115 (2015) 9869–9921.
- [63] C. Liu, L. Jing, L. He, Y. Luan, C. Li, *Chem. Commun.* 50 (2014) 1999–2001.
- [64] H. Zhang, Z. Hou, Y. Zhu, J. Wang, Y. Chen, *Appl. Surf. Sci.* 396 (2017) 560–565.
- [65] W. Song, Z. Ren, S.-Y. Chen, Y. Meng, S. Biswas, P. Nandi, H.A. Elsen, P.-X. Gao, S.L. Suib, *ACS Appl. Mater. Inter.* 8 (2016) 20802–20813.
- [66] C. Zhang, Y. Li, Y. Wang, H. He, *Environ. Sci. Technol.* 48 (2014) 5816–5822.